Methods to estimate functional and effective brain connectivity from MEG data robust to artifacts of volume conduction

Guido Nolte[1], **Laura Marzetti**[2]

[1]Dept. of Neurophysiology and Pathophysiology,
University Medical Center Hamburg-Eppendorf, Martinistr. 52, D - 20246 Hamburg, Germany
email: g.nolte@uke.de
[2]Dept. of Neuroscience and Imaging, "G. D'Annunzio" University and Institute for Advanced Biomedical Technologies, "G. D'nnunzio" University Foundation, Via dei Vestini, 66100 Chieti, Italy

Abstract Due to the high temporal resolution of MEG data they are well suited to study brain dynamics while the limited spatial resolution constitutes a major confounder when one wants the estimate brain connectivity. To very large extent, functional relationships between MEG sensors and also between estimated sources are caused by incomplete demixing of the brain sources. Many measures of functional and effective connectivity are highly sensitive to such mixting artifacts. In this bookchapter we review methods which address this problem. They are all based on the insight that the imaginary part of the cross-spectra cannot be explained as a mixing artifact. Several variants of this idea will be presented. We will present three different methods adapted to localize source interactions: a) Minimum Overlap Component Analysis (MOCA) decomposes linear estimates of the P most relevant singular vectors of the imaginary parts of the cross-spectra, b) the MUSIC algorithm can be applied to this same subspace, and c) the estimated sources can be analyzed further using multivariate generalizations of the imaginary part of coherency. Finally, a causal relation between these sources can be estimated using the Phase Slope Index (PSI). The methods will be illustrated for empirical MEG data of a single subject under resting state condition.

1 Introduction

Magnetoencephalography (MEG) and Electroencephalography (EEG) can directly measure ongoing brain activity at the temporal scale of neuronal communication, i.e. frequencies nominally in the range of 1 - 100 Hz. Although these techniques feature such a millisecond time resolution, their spatial resolution is intrinsically limited by the fact that neuronal signals are recorded from the scalp (Hari and Salmelin 2012).

In the past decades the main focus of EEG and MEG research was the analysis of event related fields, i.e. the average brain response to a given stimulus. More recently, the interest of the scientific community has moved towards the understanding of how information is integrated in the brain. Neural oscillations, which are thought to be a direct manifestation of cortical connectivity (Singer 1999; Schnitzler and Gross 2005; Varela et al. 2001), have thus become the focus of the analysis. The ability of MEG (and EEG) to study brain connectivity has been shown by a large number of studies (Fries 2009; Gow et al. 2008; Gross et al. 2002; Gross et al. 2006; Ioannides et al. 2000; Jerbi et al. 2007; Siegel et al. 2008; Wolmersdorf and Fries 2006), the great preponderance of this work still concerns coherence induced by task- or stimulus-related events. Nevertheless, strong evidence has been provided by the functional magnetic resonance (fMRI) research in the last fifteen years for the brain as an ensemble of large distributed brain networks that show patterns of coherent activity also in the absence of any imposed task or stimulus, i.e. at rest. Some of these networks are associated with simple sensory processing and others with higher level cognitive function (Buckner and Vincent 2007; Cole et al. 2010; Daglish at al. 2005; Deco and Corbetta 2010; Damoiseaux and Greicius 2009; Fox and Raichle 2007; Miller et al. 2009). Very recently it has been shown that networks can also be detected using MEG (Brookes et al. 2011a; Brookes at al. 2011b; de Pascquale et al. 2012; Liu et al. 2010). Despite these promising results, a number of methodological difficulties remain when studying brain connectivity using noninvasive electrophysiological measurements like MEG or EEG. The major challenge is that the data are largely unknown mixtures of activities of brain sources and thus spurious connectivity, which can be estimated by various measures of statistical dependencies (Pereda et al. 2005), can exist that is due entirely to signal leakage rather than to interacting sources (Brookes et al. 2012; Schoffelen and Gross 2009).

To address this issue, we suggest to construct estimates of brain connectivity from quantities that are unbiased by non-interacting sources. For zero mean data[1] the linear statistical signal properties can be determined by the cross-spectral matrices $S(f)$ defined as

$$S_{ij}(f) = \langle x_i(f) x_j^*(f) \rangle \tag{1}$$

where $x_m(f)$ are the Fourier transforms at frequency f in channel m for a given segment or trial and $\langle \cdot \rangle$ denotes the expectation value which is typically approximated by an average over the segments or trials.

It is straight forward to show that noninteracting sources do not contribute systematically, i.e. apart from random fluctuations around zero to the imaginary part of the cross-spectra, $\Im(S(f))$, regardless of the number of sources and details of the forward mapping (Nolte et al. 2004). The reason is that the forward mapping is essentially instantaneous and does not induce phase delays to excellent approximation (Stinstra and Peters 1998) which would be necessary to yield a nonvanishing imaginary part of $S(f)$.

From the cross-spectra $S(f)$ one can construct coherency matrices $C(f)$, which are a normalized version of $S(f)$, as

[1] In an event related design the mean can be subtracted.

$$C_{ij}(f) = \frac{S_{ij}(f)}{\sqrt{S_{ii}(f)S_{jj}(f)}} \tag{2}$$

In contrast to the imaginary parts of the cross-spectra, $\Im(C(f))$ also depends on independent sources through the denominator in Eq.2. However, independent sources can only lead to a decrease of $\Im(C(f))$ and hence also $\Im(C(f))$ reflects true interaction even though the physiological interpretation is not trivial especially when interpreting differences of $\Im(C(f))$ e.g. between different tasks.

Based on these observations we suggested a series of methods to identify and localize brain interactions (Nolte et al. 2006; Marzetti et al. 2008; Nolte et al. 2009; Ewald et al. 2012, Shahbazi et al. 2012). Additionally, we proposed a method to identify causal structures of the dynamical system under study (Nolte et al. 2008). We here give a brief review of some of these methods (Nolte et al. 2006; Marzetti et al. 2008; Ewald et al. 2012, Shahbazi et al. 2012; Nolte et al. 2008) to identify interacting brain sources and to estimate causal relationships. All the methods will be demonstrated using real data whose characteristics are defined in the following section.

2 Data set

For illustrative purposes, and for illustrative purposes only, we will apply the methods, which will be reviewed throughout this chapter, to an emprirical MEG data set. The data set consists of around 20 minutes MEG data, under resting state, with 10 minutes eyes closed and 10 minutes eyes open. We will average across these two conditions. MEG was measured with a CTF system with 273 channels in Hamburg-Eppendorf.

For the subject an anatomical MRI data set was available which was analyzed with fieldtrip/SPM (Oostenveld et al. 2011) for segmentation to get a volume conductor, which was defined by the inner surface of the skull. Forward calculation was done with an expansion of the magnetic lead field (Nolte 2003).

Spectral analysis was done with a frequency resolution of 0.5 Hz using short-time FFTs of Hanning windowed segments of 2 seconds duration. In Fig.1 we show the power for all channels and the imaginary part of coherency (ImCoh) for all pairs of channels as function of frequency. While the peak in the alpha range is very clear it is fairly weak in the beta range and not observable in the gamma range. The rhythms are more clear for ImCoh showing two peaks in the alpha range, at 8Hz and 10 Hz, a clear peak in the beta range, with a center at 20.5 Hz, and an additional weaker peak at 31 Hz.

In general, subjects can be very different. The present subject has prominent peaks of the imaginary part of coherency at alpha, beta, and gamma frequencies both under eyes closed and eyes open condition. The gamma peak is apparently a (second) higher harmonic of the motor alpha rhythm. At the alpha peak the distinction between central and occipital alpha is not straight forward. The beta-peak,

on the other hand, appears to be clearly related to activity in sensory-motor areas, which is also the case for the weaker gamma peak. Since we here show just one example for illustration we decided to discuss in the detail the inverse solutions for the beta-rhythm.

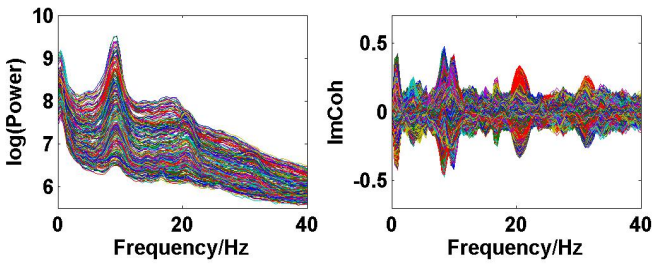

Fig. 1 Power for all channels and ImCoh for all pairs of channels.

In Fig.2 we show the imaginary part of coherency at 20.5 Hz. Each of the 50 circles represents one out of the total of 273 channels and shows its ImCoh value to all other channels. The subset of 50 equally distributed channels was chosen to ease visibility. We observe clear dipolar structures over both hemispheres, however, with unclear origin from visual inspection.

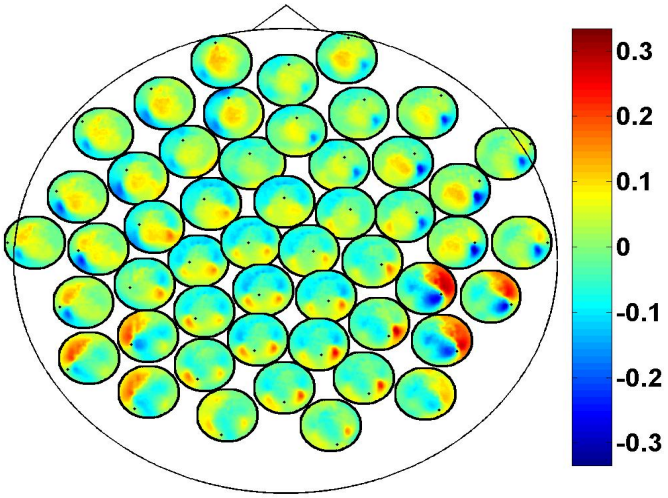

Fig. 2 ImCoh at 20.5 Hz between 50 selected channels and all other channels.

3 Methods

3.1 Identifying the subspace

Below, we will use two different inverse methods to find the sources of the imaginary part of the cross-spectrum. Both methods require the identification of a low dimensional subspace within the channel space. Analogous to the standard PCA decomposition of the full cross-spectrum of a covariance matrix we perform a singular value decomposition of the imaginary part of the cross-spectrum at the signal frequency $f = 20.5Hz$

$$S_{signal} = S(f) \tag{3}$$

For some applications it is convenient to estimate a meaningful contrast, i.e. a cross-spectrum which contains similar background noise but not the rhythmic phenomenon which is under study. We will here construct this as an interpolation between neighboring frequencies:

$$S_{noise} = \frac{1}{2}\left(S(f+\Delta f)+S(f-\Delta f)\right) \tag{4}$$

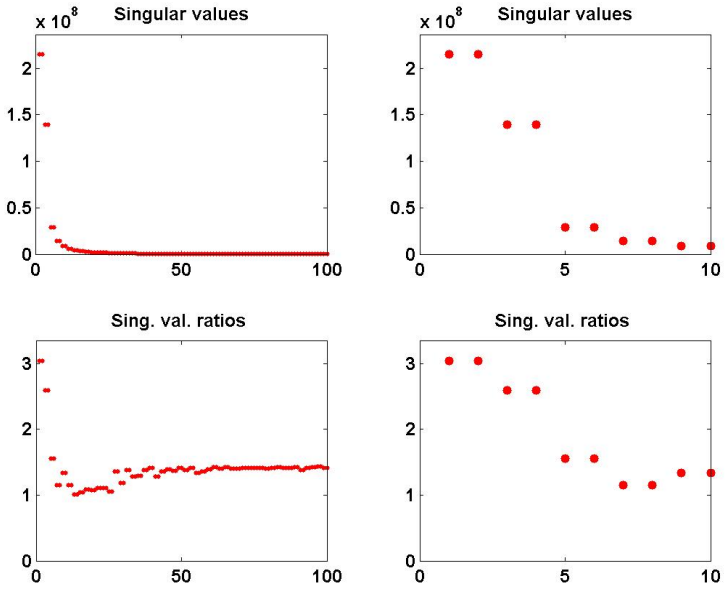

Fig. 3 Top: Singular values of imaginary part of cross-spectrum at 20.5 Hz. Bottom: Ratio of singular values of imaginary part of cross-spectrum at 20.5 Hz and a noise cross-spectrum.

The singular values of $\Im(S_{signal})$ and the ratios of these and the corresponding singular values of $\Im(S_{noise})$ are shown in Fig.3. Since the imaginary parts of cross-spectra are real valued and antisymmetric, all singular values occur in pairs. (For an odd number of channels the last one is zero.) We observe the presence of four prominent singular values. The ratios of singular values converge roughly to $1.37 \approx \sqrt{2}$, indicating that the background noise is estimated too low. This is expected if the background noise consists essentially of non-interacting sources: the linear interpolation effectively doubles the number of averages and since for non-interacting sources the imaginary part of the cross-spectrum drops with $1/\sqrt{N}$ for N averages, we expect an additional drop by a factor $\sqrt{2}$. The factor is slightly less than $\sqrt{2}$ which is possibly due to the typical $1/f$-decay of the background noise: it is a convex function having the property that linear interpolations are above the true value. Also from this ratio we observe that only 4 singular values are clearly above noise level. In the following we will always analyze this 4-dimensional subspace.

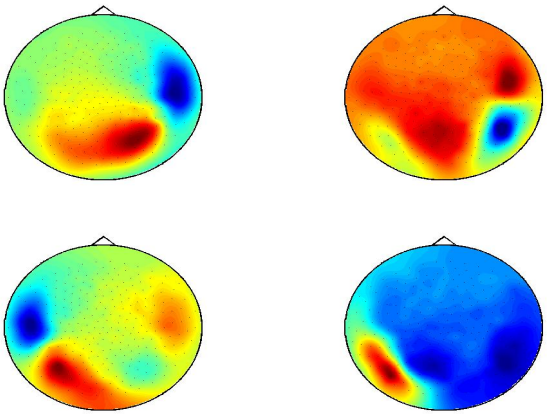

Fig. 4 First four singular vectors of the imaginary of the cross-spectrum at $f = 20.5$ Hz.

The singular vectors are shown in Fig.4. They roughly have dipole structure, but apparently the dipoles are not well separated. A standard method to demix sources is Independent Component Analysis (ICA), which, however, is not appropriate here, since we are studying interacting sources in sharp contrast to the fundamental assumption of ICA. A separation can still be done using dynamical assumptions if one assumes that all interactions are pairwise using the 'Pairwise Interacting Component Analysis' (PISA) (Nolte et al. 2006). Then the pairs can be separated from each other but a separation of the two sources within each pair is not possible. Also, for such a separation a wide-band analysis of the the data is necessary and cannot be done for a single frequency alone. For completeness, we will sketch the theory behind it, but below we will continue with the space spanned by all chosen singular vectors without dynamical separation.

In general, EEG and MEG data are a superposition of many subsystems including (effectively) independent sources but also interacting rhythmic sources of various physiological content. To separate these systems one can assume that (a) all interactions are pairwise and that (b) there are not more interacting sources than channels. These two assumptions are a clear simplification of the true brain dynamics, but they yield a unique decomposition of the data and may capture the most relevant aspects of the interaction observed in EEG/MEG data. These assumptions can be expressed for an even number of N channels as a model for the imaginary part of the cross spectra:

$$\Im(S(f)) = \sum_{k=1}^{N/2} p_k(f) \left(\mathbf{a}_k \mathbf{b}_k^T - \mathbf{b}_k \mathbf{a}_k^T \right) \tag{5}$$

For each k the set of topographies ($\mathbf{a}_k$ and $\mathbf{b}_k$) and the 'interaction spectrum' $p_k(f)$ form a - what we call - PISA-component. We note that this model is only unique up to linear mixing of the two topographies for each k. In other words, the model only identifies the 2D-subspace spanned by the two topographies and not the individual components. For technical details we refer to (Nolte et al. 2006).

3.2 Inverse method

In order to uniquely decompose the 2D-subspaces found by the singular value decomposition into contributions from individual sources we must introduce further spatial constraints on the nature of the sources. To apply a method designed to this purpose, outlined in the next section, it is necessary to use a linear inverse method. While in principle the decomposition in sensor space itself does not depend very much on the chosen inverse method, results in source space can vary substantially. We here use eLORETA (Pascual-Marqui et al. 2011), which is a non-adaptive linear inverse solver with a block-diagonal weight matrix adjusted such that the estimated source distribution has maximal power at the true source for a single dipole. The inverse method will be applied for a predefined grid of voxels in the brain. For the $m.th$ brain voxel and for the $k.th$ dipole direction and for a given forward model, eLORETA defines a spatial filter $\mathbf{G}_{mk}$, which is a column vector of N elements for N channels, such that for the data vector $\mathbf{x}(t)$ in channel space the activity of the $k.th$ dipole moment on the $m.th$ voxel is given by

$$s_{mk}(t) = \mathbf{G}_{mk}^T \mathbf{x}(t) \tag{6}$$

Due to the linearity of the inverse method, one can directly apply the spatial filters to the cross-spectra to estimate the elements of the 3×3 cross-spectral matrix $P(f,m)$ at the $m.th$ voxel at a given frequency

$$P_{kk'}(f,m) = \mathbf{G}_{mk}^T S(f) \mathbf{G}_{mk'} \tag{7}$$

The maximum eigenvalue of $P(f,m)$ is the power of the strongest dipole at that location and the corresponding eingevector is the orientation.

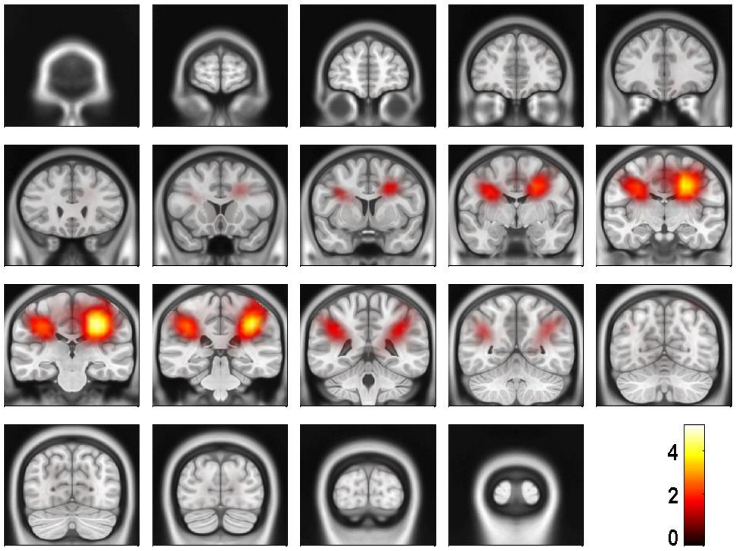

Fig. 5 Power ratio between signal and noise calculated from cross-spectra using eLORETA.

For the present data, the spectral peak in the beta range is very small. Due to the large noise, meaningful source estimates could not be achieved. Instead, it was necessary, to calculate the power in source space both for the S^{signal} and S^{noise} defined in (3) and (4) and to calculate the ratio of powers shown in Fig.5.[2] We observe signal peaks in left and right sensory-motor areas as can be expected for central beta-rhythms. We emphasize that for the estimation of the sources of the interaction, to be conducted in the nect section, the localization of power is not necessary, but only serves to demonstrate the consistency of the results.

3.3 Minimum Overlap Component Analysis (MOCA)

3.3.1 The concept

The goal of MOCA is to decompose sets of topographies based on assumptions about the underlying sources and taking note that orthogonality assumptions, as

[2] We also found that adaptive beamformer performs worse: we could not find convincing inverse solutions for both the signal power and for the power ratios.

implicit in PCA or SVD decompositions, are unrealistic (Marzetti et al. 2008). We will explain the concept for two topographies. We apply a linear inverse operator G onto the singular vectors $\mathbf{x}_1$ and $\mathbf{x}_2$, such that these topographies are mapped into distributions s_i of the source field

$$s_i = G(\mathbf{x}_i) \tag{8}$$

where $s_i = s_i(m,k)$ is a three dimensional vector field calculated in brain voxels $m = 1,..,M$ and in directions $k = 1,..,3$.

The distributions do not represent the sources of the brain, denoted as q_i, but are, within the accuracy of the inverse method, a yet unknown superposition of them:

$$s_i = \sum_{j=1}^{2} W_{ij} q_j \tag{9}$$

for $i = 1,2$. The 2×2 mixing matrix W can be calculated uniquely under the following constraints

1. The sources are orthonormal:

$$< q_i, q_j > \equiv \sum_{m,k} q_i(m,k) q_j(m,k) = \delta_{ij} \tag{10}$$

2. The sources have minimum overlap:

$$L(q_1,q_2) \equiv \sum_{m} \left(\sum_{k} q_1(m,k) q_2(m,k) \right)^2 = min \tag{11}$$

   This cost function first squares the scalar product of two dipole moments at each voxel and then sums these squares over all voxels. It vanishes if the two dipole distributions have disjoint support (i.e. disjoint regions of non-vanishing activity), thus measuring overlap. It also vanishes if the orientations at each voxel are orthogonal and therefore corresponds to a weaker form of overlap allowing in principle also activities at the same location as long as the orientations are sufficiently different. Thus, a strong bias towards remote interaction is removed.

The minimization in Eq.11 can be done analytically (Marzetti et al. 2008). If the concept is generalized to more than two topographies the minimization requires a numerical approach, which, however, is surprisingly fast and robust (Nolte et al. 2009). We note that the spatial constraints (Eq.10 and Eq.11) and the methods to solve the minimization are similar to those used in ICA in the context of fMRI data analysis (McKeown and Sejnowski 1998; Matsuda and Yamaguchi 2004) with the major difference that we here decompose vector fields rather than scalar ones. To relate to ICA to decompose EEG and MEG data, the orthogonality constraint in Eq.10 corresponds, mutatis mutandis, to 'sphering' as is used in most ICA methods: the data are transformed to be exactly uncorrelated while independence in higher statistical orders is only forced to be as good as possible.

3.3.2 Illustration

Once the demixing matrix W is found, it can be applied equally to the source distributions and the topographies. If U is an $N \times K$ matrix containing the first K singular vectors as columns, and $H = W^{-1}$ is the demixing matrix, then $\hat{U} = UH^T$ contains as columns the demixed topographies. The demixed topographies for the singular vectors shown in Fig.4 are presented in Fig.6. While, of course, the true result is not known for real data, we observe that the apparent mixture of several dipolar structures has been removed.

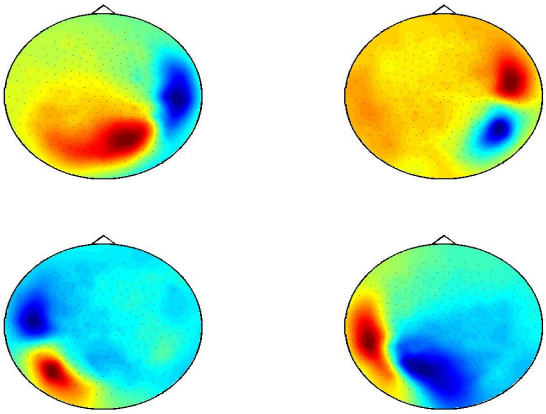

Fig. 6 Demixed singular vectors using MOCA

In Fig.7 we show the power of the source estimate for all four demixed topographies. We can see that, similar to the result shown in Fig.5, sources are located in left and right motor-sensory areas. In contrast to the localization of the entire cross-spectrum, for this localization of the interacting sources it is not necessary to visualize power ratios to achieve meaningful results.

3.3.3 Minimization of the cost function

In this subsection we present the algorithm to solve the minimization problem defined by MOCA. If we only have two source distributions this can be done analytically. To do this we first whiten the distributions s_i to fulfill (10)

$$\hat{s}_i = \sum_j A_{ij} s_j \tag{12}$$

with $A = V^{-1/2}$ and

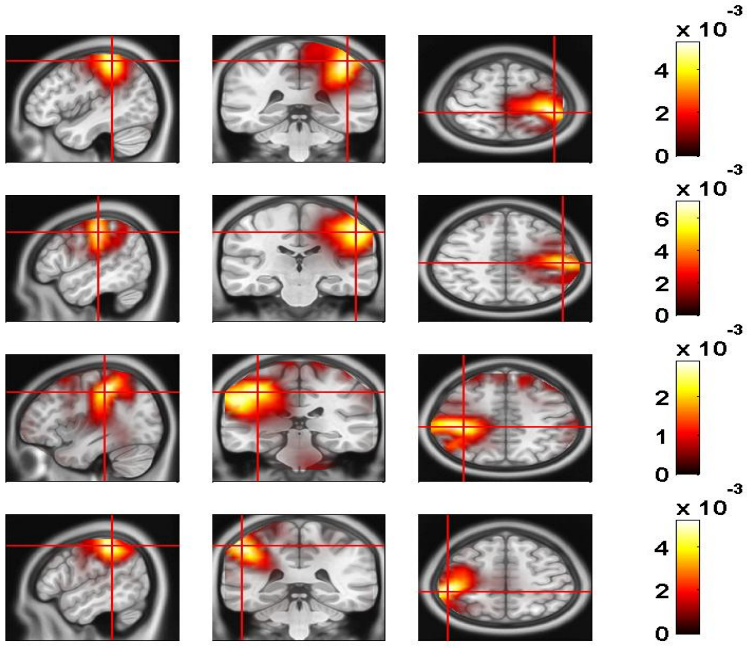

Fig. 7 Sources of demixed singular vectors. Each row displays one source distribution with shown MRI-slices centered at the maximum of the respective power distribution.

$$V_{ij} = \sum_{m,k} s_i(m,k) s_j(m,k) \tag{13}$$

In a second step we rotate $\hat{s}_i$ as

$$\begin{pmatrix} q_1 \\ q_2 \end{pmatrix} = \begin{pmatrix} \cos(\phi) & \sin(\phi) \\ -\sin(\phi) & \cos(\phi) \end{pmatrix} \begin{pmatrix} \hat{s}_1 \\ \hat{s}_2 \end{pmatrix} \tag{14}$$

and find the angle ϕ by minimizing the cost function defined in (11). This minimization can be done analytically in closed form and leads to the solution

$$\phi_0 = \frac{1}{4} tan^{-1}\left(\frac{b}{a-c}\right) \tag{15}$$

with

$$a = \sum_m \left(\sum_k \hat{s}_1(m,k)\hat{s}_2(m,k) \right)^2$$

$$b = \sum_m \left(\sum_k \hat{s}_1(m,k)\hat{s}_2(m,k) \sum_k (\hat{s}_1(m,k)\hat{s}_1(m,k) - \hat{s}_2(m,k)\hat{s}_2(m,k)) \right)$$

$$c = \frac{1}{4}\sum_m \left(\sum_k (\hat{s}_1(m,k)\hat{s}_1(m,k) - \hat{s}_2(m,k)\hat{s}_2(m,k)) \right)^2 .$$

Various solutions arise due to the various branches of the $\tan^{-1}$ function and differ by multiples of $\pi/4$. Minima and maxima are alternating, and we only have to calculate two neighboring solutions with angles ϕ_{max} and ϕ_{min} for the maximum and minimum, and pick the one referring to the minimum out of these two.

For more than two sources the cost function in (11) cannot be solved analytically and must be solved numerically with an iterative procedure using the analytic solution for any given pair of source distributions. These 'sweeps' are repeated over all pairs until convergence is reached. This procedure appears at first sight to be rather naive because such a rotation might affect overlaps between other pairs of sources. This, however, is not the case: all changes between other pairs cancel out exactly in the total cost function which results in a highly efficient algorithm with only few sweeps necessary.

3.4 MUSIC

The Multiple Signal Classification (MUSIC) algorithm is a method which finds sources based on low dimensional subspaces of the entire signals assuming that the topographies of dipoles on true source locations are contained in such a subspace. This is most commonly applied to low dimensional approximations of a covariance matrix defined by the K eigenvectors corresponding to the K largest eigenvalues. Recently, it was suggested to apply this algorithm to the K singular vectors corresponding to the K largest singular values of the imaginary part of the cross-spectrum (Shahbazi et al. 2012).

We here recall the essential steps for the MUSIC algorithm. We will at first consider the almost trivial case of fixed dipole orientations with a topography $\mathbf{L}$ and a one-dimensional subspace $\mathbf{U}$, which are both $N \times 1$ vectors. The consistency between dipole field and subspace can be measured by the angle

$$\cos\Theta = \frac{\mathbf{L}^T\mathbf{U}}{(\mathbf{L}^T\mathbf{L})^{1/2}(\mathbf{U}^T\mathbf{U})^{1/2}} \tag{16}$$

In the general case, the subspace U is an $N \times K$ matrix and L is an $N \times 3$ matrix corresponding to all three dipole orientations. The question then is whether some dipole at a specific location is consistent with the subspace, i.e. whether $L\mathbf{x}$ with unknown dipole moments $\mathbf{x}$ matches a linear combination of the columns of U, which is expressed as $U\mathbf{y}$ with $\mathbf{y}$ being an unknown $Kx1$ vector. For the minimal angle we have

$$\cos\Theta = \max_{\mathbf{x},\mathbf{y}} \frac{\mathbf{x}^T L^T U\mathbf{y}}{(\mathbf{x}^T L^T L\mathbf{x})^{1/2}(\mathbf{y}^T U^T U\mathbf{y})^{1/2}} \tag{17}$$

For later use, we express this maximization problem by a gain function $G(\mathbf{x},\mathbf{y})$ with

$$G(\mathbf{x},\mathbf{y}) = \frac{\mathbf{x}^T Z \mathbf{y}}{(\mathbf{x}^T X \mathbf{x})^{1/2} (\mathbf{y}^T Y \mathbf{y})^{1/2}} \tag{18}$$

where X and Y are symmetric and positive definite matrices. Maximization, as well as minimization, of G leads to the eigenvalue problem

$$X^{-1/2} Z Y^{-1} Z^T X^{-1/2} \hat{\mathbf{x}} = \lambda \hat{\mathbf{x}} \tag{19}$$

$$Y^{-1/2} Z^T X^{-1} Z Y^{-1/2} \hat{\mathbf{y}} = \lambda \hat{\mathbf{y}} \tag{20}$$

with

$$\hat{\mathbf{x}} = X^{1/2} \mathbf{x} \tag{21}$$

$$\hat{\mathbf{y}} = Y^{1/2} \mathbf{y} \tag{22}$$

The eigenvalues in (19) and (20) are identical, but the eigenvectors are not. If λ_{max} is the maximal eigenvalue, then G is maximized and minimized by the corresponding eigenvectors and it attains the value

$$G^2_{max} = \lambda_{max} \tag{23}$$

Whether a maximim G^2 is a maximum or minimum of G depends on the chosen sign of the eigenvectors which is arbitrary. If we have a maximum for some choice of signs we get a minimum by switching the sign of one of the eigenvectors.

The MUSIC algorithm corresponds to the above case by setting

$$X = L^T L \tag{24}$$

$$Y = U^T U = id_{K \times K} \tag{25}$$

$$Z = L^T U \tag{26}$$

For the minimal angle we get

$$\cos^2 \Theta_{min} = \lambda_{max} \tag{27}$$

and the dipole orientation $\mathbf{x}$ can be calculated from (21). Finally, the topography of the optimized dipole reads

$$\mathbf{v} = L\mathbf{x} \tag{28}$$

For a MUSIC-scan the maximal eigenvalue λ_{max} is calculated for all voxels, and displayed as $1/(1-\lambda_{max})$ which is infinite for a perfect fit.

The MUSIC algorithm can be used to find the location in the brain which is most consistent with the observed subspace as the voxel which maximizes λ_{max} now also over source points. The technical disadvantage of MUSIC is that finding several maxima may be difficult (Mosher et al. 1998). As a remedy, a modification called Recursively Applied and Projected (RAP)- MUSIC was proposed (Mosher et al. 1999). Here, instead of searching simultaneously for several local maxima, only

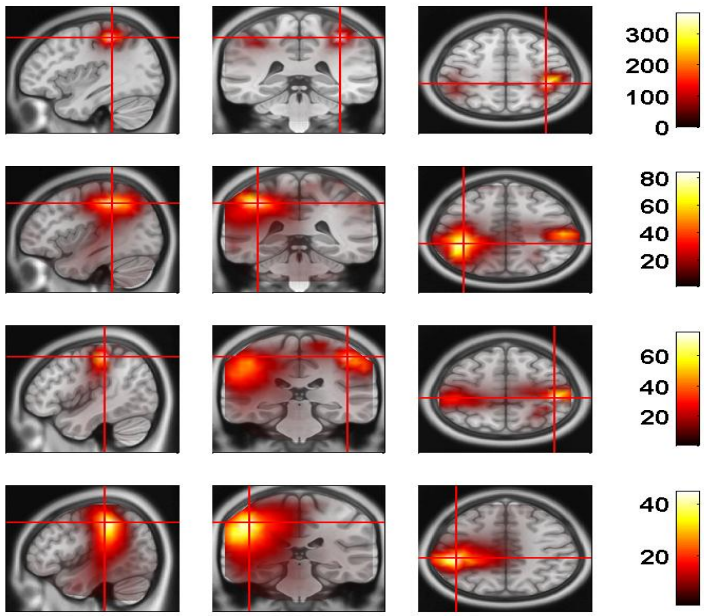

Fig. 8 RAP-MUSIC scan of imaginary part of cross-spectrum. The k.th row shows the k.th scan in the three orthogonal views.

global maxima are determined iteratively. In order to find the next source location, the subspace is updated by projecting out the previously found topographies and then the maximization is repeated. If $V = (\mathbf{v}_1, ..., \mathbf{v}_l)$ is the matrix containing as columns the topographies of l sources, then these topographies are projected out both from L and the subspace. Defining a projector as

$$P = id - V\left(V^T V\right)^{-1/2} V^T \tag{29}$$

and in order the find the $l-1.th$ location, L is replaced by PL and U is replaced by PU and then the MUSIC algorithm is applied as outlined above.

The result of RAP-MUSIC scans is shown in Fig.8 for four interations. The red crosses indicate the locations of the maximal eigenvalues which are almost identical to the maxima found by the MOCA inverse solutions. In these figures, the top row corresponds to a 'normal' MUSIC scan without projection. All locations are in principle contained in the scan but only the 'strongest' source is visible in this scan. The $i.th$ row corresponds to a MUSIC-scan after the topographies of the $i-1$ previously found sources is projected out.

3.5 ImCoh in source space

To calculate connectivity in source space we first map activities of sensors into sources using eLORETA and then we calculate the imaginary part of coherency between several sources. This is straight forward if the dipole orientation for each voxel is known: the mapping into two voxels leads to a bivariate signal for which ImCoh can be calculated. This is less trivial for unknown dipole orientation, as then each voxel consists of three signals. We will here estimate the directions for each pair voxels as those for which ImCoh is maximized (Ewald et al. 2012; Shahbazi et al. 2012; Marzetti et al. 2013). Mathematically, this is very similar to the MUSIC approach presented in the previous section.

Let F_1 and F_2, both of them being $N \times 3$ matrices, be the spatial filters (given here by eLORETA) which map the sensor activity into voxel 1 and voxel 2, respectively. If $\mathbf{x}(t)$ is the activity in the sensors, then the sources activity in the $i.th$ voxel reads

$$\mathbf{s}_i(t) = F_i^T \mathbf{x}(t) \tag{30}$$

for $i = 1,2$. Then the cross-spectral matrices within each voxel reads

$$\hat{S}_{ii}(f) = F_i^T S(f) F_i \tag{31}$$

recalling that $S(f)$ is the cross-spectrum in sensor space. The cross-spectral matrices between voxel 1 and voxel 2 reads

$$\hat{S}_{12}(f) = F_1^T S(f) F_2 \tag{32}$$

If $\mathbf{x}_i$ is the dipole moment in the $i.th$ voxel, ImCoh between the two dipoles reads

$$ImCoh = \frac{\mathbf{x}_1^T \Im\left(\hat{S}_{12}\right) \mathbf{x}_2}{\left(\mathbf{x}_1^T \hat{S}_{11} \mathbf{x}_1\right)^{1/2} \left(\mathbf{x}_2^T \hat{S}_{22} \mathbf{x}_2\right)^{1/2}} \tag{33}$$

with dependence on frequency f implicit. This, again, has the structure of (18) with the setting $Z = \Im\left(\hat{S}_{12}\right)$, $X = \hat{S}_{11}$, and $Y = \hat{S}_{22}$. The maximal imaginary coherency and the dipole orientations are then given by (19)-(22) with

$$ImCoh_{max} = \sqrt{\lambda_{max}} \tag{34}$$

In Fig.9 we show this maximizing ImCoh value between between a reference voxels and all other voxels for four different reference voxels, which were found previously from MOCA, and all other voxels. The reference voxels are indicated by blue dots. We observe that ImCoh is maximized in the vicinity of the reference voxels, indicating that the interaction is local.

Local interactions are always trivially observed if one calculates the absolute value of coherency, called coherence, which is a mixing artefact: especially the coherence between a signal and itself is always one and such a result is meaningless. The situation, however, is different when calculating the imaginary part of co-

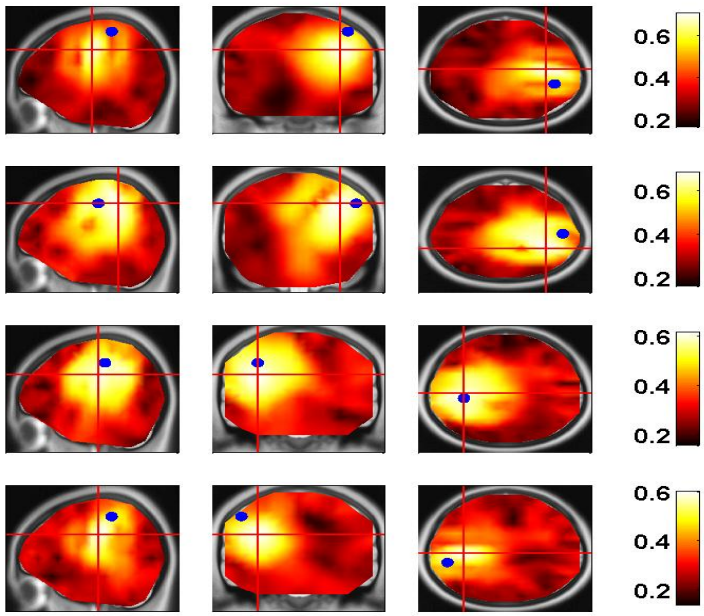

Fig. 9 Maximal ImCoh between reference voxel, calculated from MOCA, and all other voxels for four different reference voxels.

herency, which always vanishes between a signal and itself. The interaction can still come out to be local, if the true sources are very close to each other, but have different orientations. Due to the low spatial resolution of EEG/MEG inverse calculations this includes estimated interactions between a voxel and itself if the respective sources are too close to each other to be resolved. Note, that this is also the basis of the 'rotating diple model' which is an effective model for two dipoles which have such a small distance that putting them on the same location is reasonable within the limited spatial resolution of EEG/MEG data.

Had we fixed the orientation according to power, we would not be able to observe such local interactions. In Fig.10 we show results for the absolute value of imaginary part of coherency for fixed dipole orientations, chosen to the ones which maximize the power for each voxel. For the sources on the right hemisphere we get a qualitatively similar picture but with substantially suppressed values for ImCoh. The local interaction is almost completely lost on the left hemisphere and the remaining interaction appears to be too low and scattered to be considered meaningful.

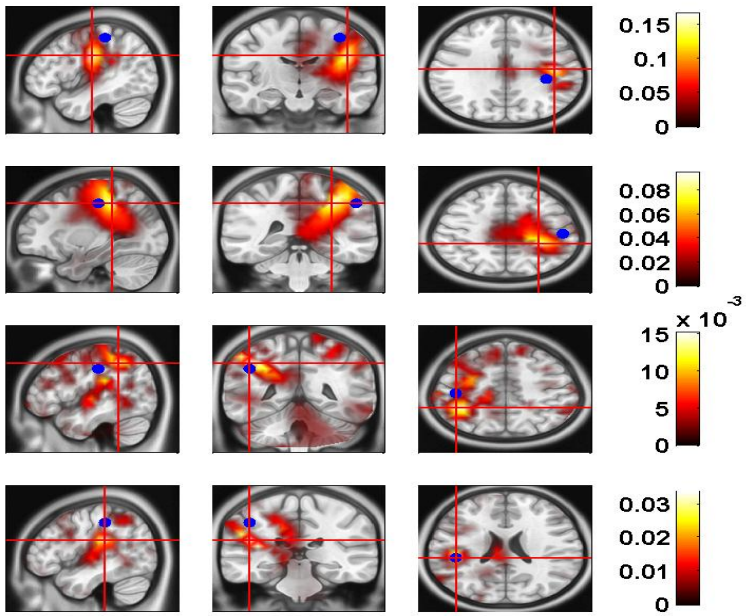

Fig. 10 ImCoh between reference voxel, calculated from MOCA, and all other voxels for four different reference voxels with dipole orientation fixed by power.

3.6 Phase Slope Index (PSI)

We finally want to estimate causal structures between the estimated sources. The 'Phase Slope Index' (PSI) estimates the causal structure between any two source activities. It is defined as (Nolte et al. 2008)

$$\hat{\Psi}_{ij} = \Im\left(\sum_{f\in F} C^*_{ij}(f)C_{ij}(f+\delta f)\right) \tag{35}$$

where $C_{ij}(f)$ is the complex coherency between sources i and j, as given in Eq.2, and δf is the frequency resolution of the coherency. F is the set of frequencies over which the slope is summed. Usually, F contains all frequencies, but it can also be restricted to a specified band for rhythmic activities.

To see that the definition of $\hat{\Psi}_{ij}$ corresponds to a meaningful estimate of the average slope it is convenient to rewrite it as

$$\hat{\Psi}_{ij} = \sum_{f\in F} \alpha_{ij}(f)\alpha_{ij}(f+\delta f)\sin(\Phi(f+\delta f)-\Phi(f)) \tag{36}$$

with $C_{ij}(f) = \alpha_{ij}(f)\exp(i\Phi(f))$ and $\alpha_{ij}(f) = |C_{ij}(f)|$ being frequency dependent weights.
For smooth phase spectra, $\sin(\Phi(f+\delta f) - \Phi(f)) \approx \Phi(f+\delta f) - \Phi(f)$ and hence $\hat{\Psi}$ corresponds to a weighted average of the slope.

We list the most important qualitative properties of $\hat{\Psi}$:

1. For an infinite amount of data and for arbitrary instantaneous mixtures of an arbitrary number of independent sources, $\hat{\Psi}$ is exactly zero, because mixtures of independent sources do not induce an imaginary part of coherencies (Nolte et al. 2004)) which in turn is necessary to generate a non-vanishing $\hat{\Psi}$. For finite data, $\hat{\Psi}$ will then fluctuate in this case around zero within error bounds. A special case of this are phase jumps from 0 to $\pm\pi$ which can arise also for mixtures of independent sources.
2. $\hat{\Psi}$ is expressed in terms of coherencies, only. The standard deviation of a coherency is approximately constant and only depends on the number of averages which is equal for all frequencies. Thus, large but meaningless phase fluctuations in frequency bands containing essentially independent signals are largely suppressed.
3. If the phase $\Phi(f)$ is linear in f and provided that the frequency resolution is sufficient (i.e. δf is sufficiently small), the argument in the sum has the same sign across all frequencies and then $\hat{\Psi}$ will have the same sign as the slope of $\Phi(f)$.

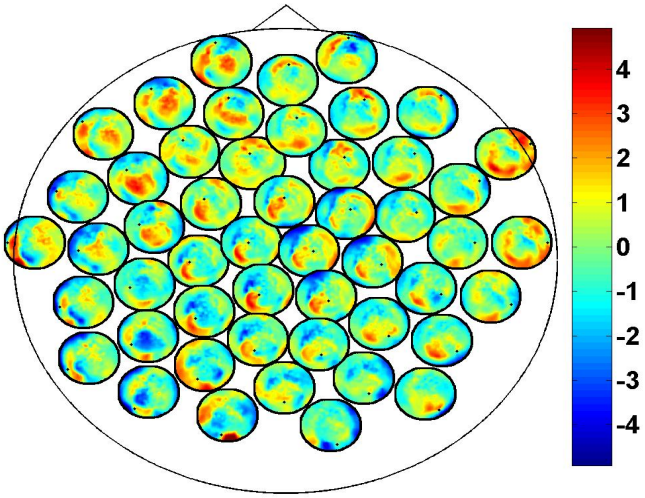

Fig. 11 PSI in channel space.

It is convenient to normalize $\hat{\Psi}$ by an estimate of its standard deviation

$$\Psi = \frac{\hat{\Psi}}{std(\hat{\Psi})} \tag{37}$$

with $std(\hat{\Psi})$ being estimated by the Jackknife method. In the examples below we consider absolute values of each larger than 2 as significant.

It is important to point out that the phase of coherency itself is not interpreted in terms of causality. For example, a phase of $\pi/2$ switches to $-\pi/2$ if the sign of one of the signals is reversed, but the PSI measure is invariant with respect to the sign of the signals. Rather than on phase, PSI is based on the slope of the phase as a function of frequency. Note, that a sign change adds a constant to the phase and has no effect on the slope. The method assumes that the studied frequency range properly covers the dynamical range. For purely periodic signals, any causality estimate would be dubious. In that case Ψ would be insignificant because negative and positive slopes cancel.

To calculate the causal relation for the beta range we calculated PSI in the frequency range around the beta peak $[f-\Delta f, f+\Delta f]$ with $f = 20.5Hz$ and $\Delta f = 2Hz$. Results in channel space are shown in Fig.11. Absolute values of PSI above 2 are signicant without correction for multiple comparison with $p \leq .05$. We observe fairly large values values up to almost 5 but with highly unclear spatial structure.

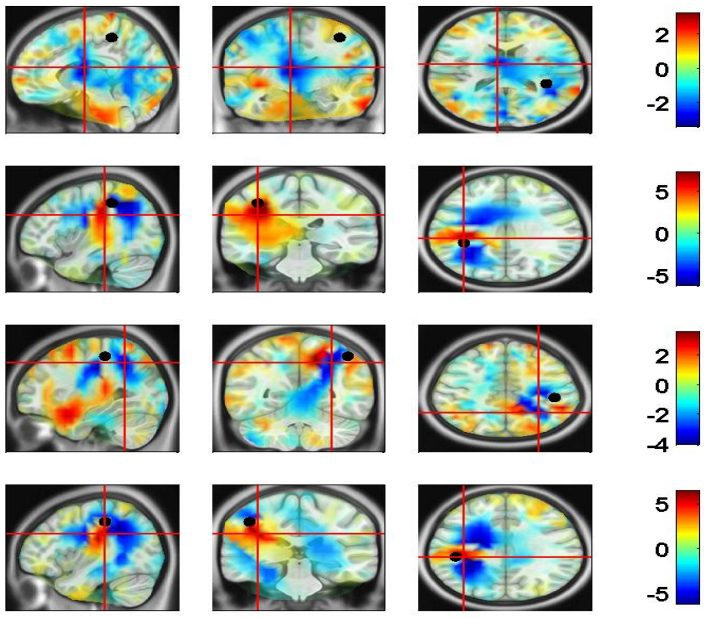

Fig. 12 PSI between reference voxel (black dot) and all other voxels for four different references. Blue color means the reference is receiving information from these areas and red means the reference is sending information to these areas.

To calculate PSI in source space we need to fix an orientation of the dipoles. For each pair of voxels these orientations are chosen to maximize imaginary coherence between the voxels at frequency $f = 20.5Hz$ as explained in the previous section. Results for reference voxels taken from results of the RAP-MUSIC algorithm are presented in Fig.12. We observe higher (and hence more significant) values than on the sensor level which can mainly be explained by the fact that the source orientation was optimized to observe delayed interactions.

In contrast to ImCoh, for which we displayed the absolute value, the result now has a sign. Such a sign was meaningless for ImCoh at the source level, because it switches if we switch the sign of a source. Since the dipole moment was calculated by an eigenvalue equation with meaningless sign of the eigenvector such a sign was also meaningless for ImCoh. In contrast, PSI does not depend on the sign of the dipole but reflects temporal order. In the figure, blue regions mean that the reference voxel receives information from them, while the reference voxel send information to the red ones. We emphasize, that maximizing ImCoh does not necessarily maximize PSI. It is very well possible that the present approach still misses major effects which are bigger than the ones observed.

4 Conclusion

We presented a series of methods to study functional and effective connectivity from MEG/EEG data in the frequency domain. All presented methods addressed the problem of volume conduction which is by far the most severe confounder when one wants to estimate brain interactions. The basis of the methods is the observation that brain interactions take some time which is much longer than the time needed for the propagation of electromagnetic signals from a source to a sensor which can be considered as quasi-instantaneous for the frequency ranges of interest (Stinstra and Peters 1998). The finite time needed for different neuronal groups to interact with each other makes it possibile to find true brain interactions by systematically exploiting time delays between measured signals. This, however, does not mean that for any brain interaction the time delay is observable. If, e.g., an interaction is totally symmetric all net phase/time delays vanish and the interaction cannot be studied with these methods.

We presented two different methods, MOCA and RAP-MUSIC, to localize interacting sources both based on a singular value decomposition of the imaginary part the cross-spectrum at some frequency. The crucial step is to determine a low dimensional subspace of the signal space spanned by the singular vectors corresponding to the largest P singular values. The choice of P, which corresponds here to the chosen number of sources, is the only free parameter of the methods. For the chosen data set we observed a drop of the $k.th$ singular value to a noise floor for $k > 4$ and set $P = 4$ accordingly. The evaluation of other or the development of new techniques to choose P is beyond the scope of this book chapter.

Both presented inverse method only depend on the subspace spanned by the singular vectors and not on the vectors themselves. It is therefore irrelevant whether the singular vectors themselves correspond to topographies of the single sources. The first method, MOCA, is based on some linear inverse method for which we chose eLORETA, but other choices are also possible. MOCA demixes the singular vectors based on assumptions in source space. The second method was RAP-MUSIC applied to this subspace and it assumes that the interacting sources are dipoles. We then found final results to be almost identical for the two methods for the data at hand. Interactions between voxels in the brain were estimated using a multivariate method, with optimized source orientation for each voxel, which was capable of detecting both local and non-local interactions. A comparison with a bivariate method for which source orientation was fixed by power showed that the latter procedure suppresses local interactions. This could lead to a potential bias towards remote interaction. We finally estimated causal relations using the Phase Slope Index in source space with reference voxels chosen from the preceding localization of interacting sources. We observed clear and significant structures in source space which could not be expected from sensor space results.

This book chapter is not an attempt to review all methods addressing the problem of volume conduction. We concentrated on own methods, covering these only partly and totally ignoring a couple of new approaches from other researchers (Pascual-Marqui et al. 2011; Vinck et al. 2011; Stam et al. 2007; Hipp et al. 2012; Meinecke et al. 2012; Sekihara et al. 2011). The relation between our work and the nonlinear measures presented in (Vinck et al. 2011) and the multivariate measures in ((Pascual-Marqui et al. 2011) were presented in (Ewald et al. 2012). A more complete survey and comparison of all methods will be addressed in the future.

Acknowledgements

This work was supported by grants from the EU (ERC-2010- AdG-269716), the DFG (SFB 936/A3), the BMBF (031A130) and from the Human Connectome Project (1U54MH091657-01) from the 16 National Institutes of Health Institutes and Centers that support the NIH Blueprint for Neuroscience Research.

5 References

Brookes MJ, Hale JR, Zumer JM, Stevenson CM, Francis ST, Barnes GR, Owen JP, Morris PG, Nagarajan SS (2011a) Measuring functional connectivity using MEG: methodology and comparison with fcMRI. NeuroImage 56:1082-104.

Brookes MJ,Woolrich M, Luckhoo H, Price D, Hale JR, Stephenson MC, Barnes GR, Smith SM, Morris PG (2011b) Investigating the electrophysiological

basis of resting state networks using MEG. Proc. Natl. Acad. Sci. U.S.A. 108: 16783-8.

Brookes MJ, Woolrich M, Barnes GR (2012) Measuring functional connectivity in MEG: A multivariate approach insensitive to linear source leakage. Neuroimage 63: 910-20.

Buckner RL, Vincent JL (2007) Unrest at rest: default activity and spontaneous network correlations. Neuroimage 37:1091-6.

Cole DM, Smith SM, Beckmann CF (2010) Advances and pitfalls in the analysis and interpretation of resting-state FMRI data. Front Syst Neurosci. 4:8.

Daglish M, Lingford-Hughes A, Nutt D. (2005) Human functional neuroimaging connectivity research in dependence. Rev Neurosci. 16(2):151-7

Damoiseaux JS, Greicius MD. (2009) Greater than the sum of its parts: a review of studies combining structural connectivity and resting-state functional connectivity. Brain Struct Funct. 213(6):525-33.

Deco G and Corbetta M (2010) The Dynamical Balance of the Brain at Rest. Neuroscientist 17: 107-123.

de Pasquale F, Della Penna S, Snyder AZ, Lewis C, Mantini D, Marzetti L, Belardinelli P, Ciancetta L, Pizzella V, Romani GL, Corbetta M (2010) Temporal dynamics of spontaneous MEG activity in brain networks. Proc Natl Acad Sci U S A. 107:6040-5.

de Pasquale F, Della Penna S, Snyder AZ, Marzetti L, Pizzella V, Romani GL, Corbetta M (2012) A cortical core for dynamic integration of functional networks in the resting human brain. Neuron. 74:753-64.

Ewald A, Marzetti L, Zappasodi F, Meinecke FC, Nolte G. (2012) Estimating true brain connectivity from EEG/MEG data invariant to linear and static transformations in sensor space. Neuroimage. 60(1):476-88.

Fox MD and Raichle ME (2007) Spontaneous fluctuations in brain activity observed with functional magnetic resonance imaging. Nat Rev Neurosci. 8:700-11.

Fries P (2009) Neuronal gamma-band synchronization as a fundamental process in cortical computation. Annu Rev Neurosci. 32:209-24.

Gow DW, Segawa JA, Ahlfors SP, Lin FH (2008) Lexical influences on speech perception: a Granger causality analysis of MEG and EEG source estimates. Neuroimage 43:614-23.

Gross J, Timmermann L, Kujala J, Dirks M, Schmitz F, Salmelin R, Schnitzler A (2002) The neural basis of intermittent motor control in humans. Proc. Natl. Acad. Sci. U. S. A. 99:2299-302.

Gross J, Schmitz F, Schnitzler I, Kessler K, Shapiro K, Schnitzler A (2006) Anticipatory control of long range phase synchronization. Europ J Neurosci. 24: 2057-60.

Hari R and Salmelin R (2012) Magnetoencephalography: From SQUIDs to neuroscience. NeuroImage 61: 386-96.

Hipp JF, Hawellek DJ, Corbetta M, Siegel M, Engel AK (2012) Large-scale cortical correlation structure of spontaneous oscillatory activity. Nat Neurosci. 15:884-90.

Ioannides AA, Liu LC, Kwapien J, Drozdz S, Streit M (2000) Coupling of regional activations in a human brain during an object and face affect recognition task. Hum. Brain Mapp. 11, 77-92.

Jerbi K, Lachaux JP, N'Diaye K, Pantazis D, Leahy RM, Garnero L, Baillet S (2007) Coherent neural representation of hand speed in humans revealed by MEG imaging. Proc. Natl. Acad. Sci. U. S. A. 104, 7676-81.

Liu Z, Fukunaga M, de Zwart JA, Duyn JH (2010) Large-scale spontaneous fluctuations and correlations in brain electrical activity observed with magnetoencephalography. Neuroimage 51: 102-11.

Marzetti L, Del Gratta C, Nolte G (2008) Understanding brain connectivity from EEG data by identifying systems composed of interacting sources. Neuroimage 42:87-98.

Marzetti L, Della Penna S, Snyder AZ, Pizzella V, Nolte G, de Pasquale F, Romani GL, Corbetta M (2013) Frequency specific interactions of MEG resting state activity within and across brain networks as revealed by the multivariate interaction measure. Neuroimage 79:172-83.

Matsuda Y, Yamaguchi, K (2004) Semi-invariant function of Jacobi algorithm in independent component analysis. In: Neural networks, proceedings. IEEE international joint conference;

McKeown MJ, Sejnowski TJ (1998) Independent component analysis of fMRI data: examining the assumptions. Hum Brain Mapp. 6:368-72.

Meinecke F, Ziehe A, Kurths J, Müller KR (2005) Measuring Phase Synchronization of Superimposed Signals. Physical Review Letters. 94:084102

Miller KJ, Weaver KE, Ojemann JG (2009) Direct electrophysiological measurement of human default network areas. Proc Natl Acad Sci U S A. 106:12174-7

Mosher JC, Baillet S, Leahy RM (1998) EEG source localization and imaging using multiple signal classification approaches. J Clin Neurophysiol. 16:225-38.

Nolte G (2003) The magnetic lead field theorem in the quasi-static approximation and its use for magnetoencephalography forward calculation in realistic volume conductors. Phys Med Biol. 21;48(22):3637-52.

Nolte G, Bai U, Weathon L, Mari Z, Vorbach S, Hallet M (2004) Identifying true brain interaction from EEG data using the imaginary part of coherency. Clin. Neurophysiol. 115: 2294-2307.

Nolte G, Meinecke FC, Ziehe A, Müller KR (2006) Identifying interactions in mixed and noisy complex systems. Phys. Rev. E 73: 051913.

Nolte G, Ziehe A, Nikulin VV, Schlögl A, Krämer N, Brismar T, Müller KR (2008) Robustly estimating the flow direction of information in complex physical systems. Phys Rev Lett. 100:234101.

Nolte G, Marzetti L, Valdes Sosa P (2009) Minimum Overlap Component Analysis (MOCA) of EEG/MEG data for more than two sources. J Neurosci Methods. 183:72-6.

Oostenveld R, Fries P, Maris E, and Schoffelen JM (2011) FieldTrip: Open Source Software for Advanced Analysis of MEG, EEG, and Invasive Electrophys-

iological Data Computational Intelligence and Neuroscience, vol. 2011, Article ID 156869

Pascual-Marqui RD, Lehmann D, Koukkou M, Kochi K, Anderer P, Saletu B, Tanaka H, Hirata K, John ER, Prichep L, Biscay-Lirio R, Kinoshita T (2011) Assessing interactions in the brain with exact low-resolution electromagnetic tomography. Philos Transact A Math Phys Eng Sci. 13;369(1952):3768-84.

Pereda E, Quiroga RQ, Bhattacharya J (2005) Nonlinear multivariate analysis of neurophysiological signals. Prog Neurobiol. 2005 Sep-Oct;77(1-2):1-37.

Schnitzler A and Gross J (2005) Normal and pathological oscillatory communication in the brain. Nat. Rev. Neurosci. 6(4):285-96

Schoffelen JM and Gross J (2009) Source connectivity analysis with MEG and EEG. Human Brain Mapping. 30:1857-1865.

Sekihara K, Owen JP, Trisno S, Nagarajan SS (2011) Removal of spurious coherence in MEG source-space coherence analysis. IEEE Trans Biomed Eng. 58:3121-9.

Shahbazi Avarvand F, Ewald A, Nolte G. (2012) Localizing true brain interactions from EEG and MEG data with subspace methods and modified beamformers. Comput Math Methods Med. 2012:402341.

Siegel M, Donner TH, Oostenveld R, Fries P, Engel AK (2008) Neuronal synchronization along the dorsal visual pathway reflects the focus of spatial attention. Neuron. 60(4): 709-19.

Singer W (1999) Neuronal synchrony: a versatile code for the definition of relations? Neuron 24, 49-65.

Stam CJ, Nolte G, Daffertshofer A (2007) Phase lag index: assessment of functional connectivity from multi channel EEG and MEG with diminished bias from common sources. Hum Brain Mapp. 28:1178-93.

Stinstra JG, Peters MJ (1998) The volume conductor may act as a temporal filter on the ECG and EEG. Med Biol Eng Comput. 36:711-6.

Varela F, Lachaux J, Rodriguez E, Martinerie J (2001) The brain web: phase synchronization and large-scale integration. Nat Rev Neurosci. 2:229-39.

Vinck M, Oostenveld R, van Wingerden M, Battaglia F, Pennartz CM (2011). An improved index of phase-synchronization for electrophysiological data in the presence of volume-conduction, noise and sample-size bias. Neuroimage. 55:1548-65

Womelsdorf T, Fries P (2006) Neuronal coherence during selective attentional processing and sensory-motor integration. J Physiol Paris. 100:182-93.